The Effects of Cold Work on the Microstructure and Mechanical Properties of Intermetallic Strengthened Alumina-Forming Austenitic Stainless Steels

B. HU, G. TROTTER, IAN BAKER, M.K. MILLER, L. YAO, S. CHEN, and Z. CAI

In order to achieve energy conversion efficiencies of >50 pct for steam turbines/boilers in power generation systems, materials are required that are both strong and corrosion-resistant at >973 K (700 °C), and economically viable. Austenitic steels strengthened with Laves phase, NiAl and Ni_3Al precipitates, and alloyed with aluminum to improve oxidation resistance, are potential candidate materials for these applications. The microstructure and microchemistry of recently developed alumina-forming austenitic stainless steels have been characterized by scanning electron microscopy, transmission electron microscopy, and synchrotron X-ray diffraction. Different thermo-mechanical treatments were performed on these steels to improve their mechanical performance. These reduced the grain size significantly to the nanoscale (~100 nm) and the room temperature yield strength to above 1000 MPa. A solutionizing anneal at 1473 K (1200 °C) was found to be effective for uniformly redistributing the Laves phase precipitates that form upon casting.

DOI: 10.1007/s11661-015-2981-6

I. INTRODUCTION

THE energy efficiency of fossil fuel-fired boiler/steam turbine power plants is strongly dependent on the operating temperature and pressure. Hence, it is beneficial to run such power plants at higher temperatures and pressures to enhance efficiency and reduce CO_2 emissions. A key aspect for achieving this goal is the materials that are used for construction of the boilers and steam turbines.[1–3] Thus, extensive efforts are underway to develop affordable materials with the necessary strength, oxidation resistance, and corrosion resistance for operation at temperature greater than 973 K (700 °C).[4–6] High-nickel alloys and nickel-based superalloys meet all the performance goals, but are too expensive.[7–9]

Face-centered cubic (f.c.c.) austenitic stainless steels are potential materials for this high temperature application. They have a combination of good high-temperature creep strength and oxidation resistance with a relatively low cost.[3,10] To that end, a family of inexpensive, high creep strength, alumina-forming austenitic (AFA) stainless steels has recently been developed.[3,11–21] The development is based on the discovery that a protective alumina scale can be formed at 923 K to 1073 K (650 °C to 800 °C) with 2.5 wt pct Al.[3,13,16,22] The best materials recently developed have creep rupture lifetimes >3000 hours at 1023 K (750 °C) and 100 MPa, nearly 20 times longer than commercially available Fe-based Superalloy A286 (Fe-14.5Cr-25Ni-2.1Ti-0.15Al). They also show much better oxidation resistance compared to chromia-forming A286 at 1073 K (800 °C) in air containing 10 pct water vapor.[20] These recently developed alloys are based on Fe-14Cr-32Ni-3Nb-3Al-2Ti (wt pct) with various minor, but important, elemental additions. The addition of Nb is important to improve the stability of alumina scale at high temperature, and results in the formation of Fe_2Nb Laves phase.[20] The addition of Ti enhances the stability of $Ni_3(Al, Ti)$ phase in AFA alloys.[20]

In addition to Fe_2Nb Laves phase and $L1_2$ (ordered f.c.c.) Ni_3Al-type phase precipitates, a B2 (ordered b.c.c.) NiAl phase and MC carbides are observed in these AFA stainless steels.[22] The volume fractions of these phases depend on the alloy composition, mainly the Al and Nb contents. The addition of Nb is necessary to enhance the stability of the alumina scale formed at high temperature, and results in the formation of the C14 Fe_2Nb Laves phase.[3,13,16,20] The Fe_2Nb precipitates, which are stable up to 1900 K (1627 °C), are expected to be in equilibrium with both NbC and the f.c.c. iron matrix.[12,15] After an aging treatment at 1023 K (750 °C), NiAl type B2 phase precipitates can also be observed, although these have been reported to be ineffective for improving the yield strength of austenitic stainless steels above 673 K (400 °C).[5,18] However, they may enhance the creep resistance by affecting dislocation climb. Creep testing at 1023 K (750 °C) results in a finer and denser distribution of

B. HU and G. TROTTER, Ph.D. Students, and IAN BAKER, Sherman Fairchild Professor of Engineering, are with the Thayer School of Engineering, Dartmouth College, Hanover, NH 03755. Contact e-mail: ian.baker@dartmouth.edu M.K. MILLER, formerly Corporate Fellow with the Center for Nanophase Materials Sciences, Oak Ridge National Laboratory, Oak Ridge, TN 37831, is now Retired. L. YAO, Research Associate, is with the Materials Science and Technology Division, Oak Ridge National Laboratory, Oak Ridge, TN 37831. S. CHEN, Assistant Physicist, and Z. CAI, Physicist, are with the X-ray Science Division, Advanced Photon Source, Argonne National Laboratory, Argonne, IL 60439.
Manuscript submitted May 5, 2014.

Published online: 12 June 2015

these secondary precipitates than in alloys that have simply been aged at the same temperature. Such fine-scale second-phase precipitates may be effective in further increasing the creep strength.[22] The NiAl B2 phase precipitates also play an important role in the oxidation resistance since they act as an Al reservoir for forming an alumina scale at high temperatures.[23]

As both Fe_2Nb and NiAl precipitates demonstrate limited effects on the high-temperature strength at or above 923 K (650 °C),[20] the development of the AFA stainless steels has focused on introducing fine coherent precipitates such as $L1_2$-type precipitates.[20,22] Coherent Ni_3Al precipitates are effective for improving the high-temperature mechanical properties in various nickel- and iron-based superalloys. One example is the iron-based superalloy A286, which shows good creep properties due to the formation of coherent $L1_2$ Ni_3Ti precipitates at ~1003 K (730 °C). However, the strengthening effect of Ni_3Ti is limited because it is metastable at higher temperatures.[24,25] Coherent Ni_3Al precipitates in AFA stainless steels[14] have been optimized to maximize their stability to improve creep performance.[20]

Cold work with 10 pct thickness reduction can also be effective for improving the creep properties of these AFA stainless steels[22,26–28] with the dislocations introduced during cold rolling acting as nucleation sites for MC (NbC) carbide precipitates, resulting in doubled creep lives at 1023 K (750 °C).[12,15]

The current study investigated the effect of severe cold work with 90 pct thickness reduction on the microstructure and mechanical properties of recently developed AFA stainless steels, specifically the Fe-14Cr-32Ni-3Nb-3Al-2Ti wt pct-based AFA alloys. Detailed microstructural analysis was performed on the samples before and after thermo-mechanical treatments.

II. EXPERIMENTAL

The AFA stainless steels used in this study were obtained from Oak Ridge National Laboratory (ORNL). Ingots of the alloys had been hot-rolled at 1373 K (1100 °C) (80 pct thickness reduction with ~15 to 20 pct thickness reduction per pass) and then annealed at 1373 K (1100 °C) for 30 minutes in Ar + 4 pct H_2 gas, followed by air-cooling. The nominal and analyzed chemistry of the AFA stainless steel, referred to as DAFA29, are given in Table I. The chemical composition of these two alloys was analyzed using inductively coupled plasma spectroscopy and gas combustion techniques at ORNL.[29]

The microstructures of the specimens before and after thermo-mechanical processing were examined by scanning electron microscopy (SEM), transmission electron microscopy (TEM), and synchrotron-based X-ray diffraction (XRD).

For examination in the SEM, samples were polished using increasingly fine grades of silicon carbide papers and then further polished using 0.3 μm alumina powders to obtain a mirror finish. The polished samples were etched using 4 pct nitric acid for 5 seconds followed by rinsing in water. The specimens were then examined in an FEI XL-30 field emission gun (FEG) SEM operated at 15 keV.

Thin foils for TEM examination were produced from 3-mm dia., 200-μm-thick disks by twin-jet electropolishing at 11 V and ~200 mA in a solution of 25 pct nitric acid in methanol at 253 K (−20 °C) using a Struers Tenupol 5. The resulting thin foils were examined with an FEI Tecnai F20 FEG TEM operated at 200 kV and equipped with energy-dispersive X-ray spectroscopy (EDS).

Thin foil specimens were polished from 200 μm thick disks to a thickness of 20 μm for synchrotron XRD measurements. The XRD experiments were performed at the Advanced Photon Source (APS) at Argonne National Laboratory, with the X-ray microdiffraction facility at undulator beamline 2-ID-D.[30] X-ray photons with energy of 18 keV (wavelength = 0.688 nm) were selected using a Si ⟨111⟩ double-crystal monochromator, and then focused to a circular spot of ~400 nm through a Fresnel zone plate. The diffraction signals were collected with a Rayonix Mar165 CCD detector, with 2048 × 2048 pixels and 80 micron pixel size, located ~58 mm downstream of the sample. The total counting time was 55 seconds. Over this counting period, the sample was continuously rotated around an axis perpendicular to the incident beam by 110 deg.

Two thermo-mechanical treatments of the AFA stainless steel DAFA29 were performed. A detailed flowchart of these two thermo-mechanical treatments is shown in Figure 1. In Method #1, DAFA29 was cold rolled to a 90 pct reduction in thickness with a ~4.5 pct reduction per pass and then heat-thermal treated at 1073 K (800 °C) for 2.4, 24, or 240 hours. In Method #2, the alloy is given a solutionizing anneal at 1473 K (1200 °C) and then cold rolled to a 90 pct reduction in thickness with a ~4.5 pct reduction per pass before annealing at 1073 K (800 °C) for 2.4, 24, or 240 hours.

After thermo-mechanical processing, room temperature tensile tests were performed with a Hydraulic MTS testing machine. A preload force of 100 N was applied before the tensile tests were started. The initial strain rate for all tensile tests was 5×10^{-4} s^{-1}. The tensile test specimens are dog-bone geometry with a gage length of 10 mm. They were polished using 800 grit silicon carbide papers and finished with 0.3 μm alumina powders to a

Table I. Analyzed Chemistry (Weight Percent) of DAFA29[29]

Alloys	Fe	Cr	Mn	Ni	Cu	Al	Si	Nb	V	Ti	Mo	W	Zr	C	B	P	N
DAFA29																	
Nominal	45.44	14		32		3	0.15	3		2			0.3	0.1	0.01		
Analyzed	45.34	13.83	0.13	32	0.12	3.02	0.15	2.87	<0.01	2	0.1	<0.01	0.32	0.11	0.0085	<0.005	<0.0001

mirror finish. The elongations were measured directly from the specimens after the tensile tests.

In order to compare the simple annealed samples (without cold rolling) to thermo-mechanical-treated DAFA29, another two group of DAFA29 alloys were annealed as control samples. The first group (Method #1 control) samples were annealed at 1073 K (800 °C) for 2.4, 24, or 240 hours. The second group (Method #2 control) samples were annealed at 1473 K (1200 °C) and then post annealed at 1073 K (800 °C) for 2.4, 24, or 240 hours. The room temperature tensile tests of these two groups of control samples were also performed under the same test conditions.

III. RESULTS AND DISCUSSION

A. *As-received Microstructures*

A backscattered electron (BSE) image of the as-received DAFA29 showing the grain structure and the precipitates is shown in Figure 2(a). EDS data acquired from the precipitates and the matrix are shown in Figures 2(b) and (c), respectively. The white precipitates are niobium enriched consistent with a Fe_2Nb Laves phase. The Laves phase precipitates are aligned along the rolling direction, as shown in Figure 2(a) (white arrow). They are observed both on the grain boundary as well as in the interior of the grains. The size of these Laves phase is in the range 0.5 to 10 μm. Previous research suggested that the strengthening effect of Laves phase strongly depends on its size and distribution.[14] It has been predicted that better creep resistance could be obtained with further refinement and stabilization of the Fe_2Nb particle sizes to ~100 nm.[14] MC carbides (M: Nb, Ti) are also observed in DAFA29. These precipitates are randomly distributed in the matrix with a size of ~5 μm. They normally have a blocky morphology. The predicted volume fraction of this phase is around 1 pct based on JMatPro simulation.

A bright field (BF) TEM image of a precipitate in DAFA29 located on the edge of a thin foil is shown in Figure 3(a). A selected area diffraction (SAD) pattern taken from the f.c.c. matrix (lower circle in Figure 3(a)) is shown in Figure 3(b). The diffraction pattern consists of two sets of different diffraction spots, which are superimposed diffraction patterns from the $L1_2$ phase and the f.c.c. matrix. The weak diffraction spots are superlattice reflections from the $L1_2$ phase, whereas the strong diffraction spots are from both the fundamental reflections from an $L1_2$ phase and the f.c.c. matrix. The orientation relationship between the $L1_2$ phase and the f.c.c. matrix is cube-on-cube. The superlattice reflection is similar to the diffraction spots observed in previous studies on similar alloys strengthened by nanoscale coherent $L1_2$-ordered intermetallic γ'-$Ni_3(Al, Ti)$ precipitates.[20] A convergent beam electron diffraction (CBED) pattern from the large precipitate viewed along [0001] (after tilting) is shown in Figure 3(c). It shows a hexagonal pattern. Based on this result and previous

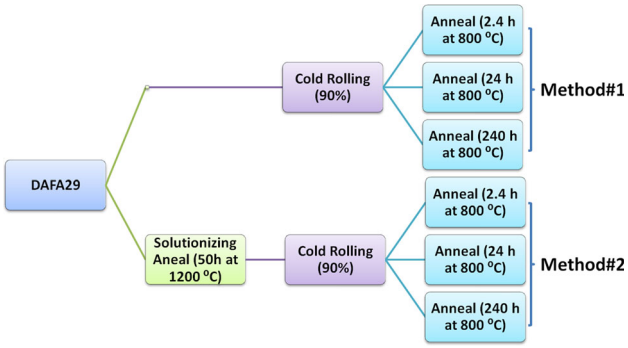

Fig. 1—Flowchart of the two thermo-mechanical treatment methods used on DAFA 29.

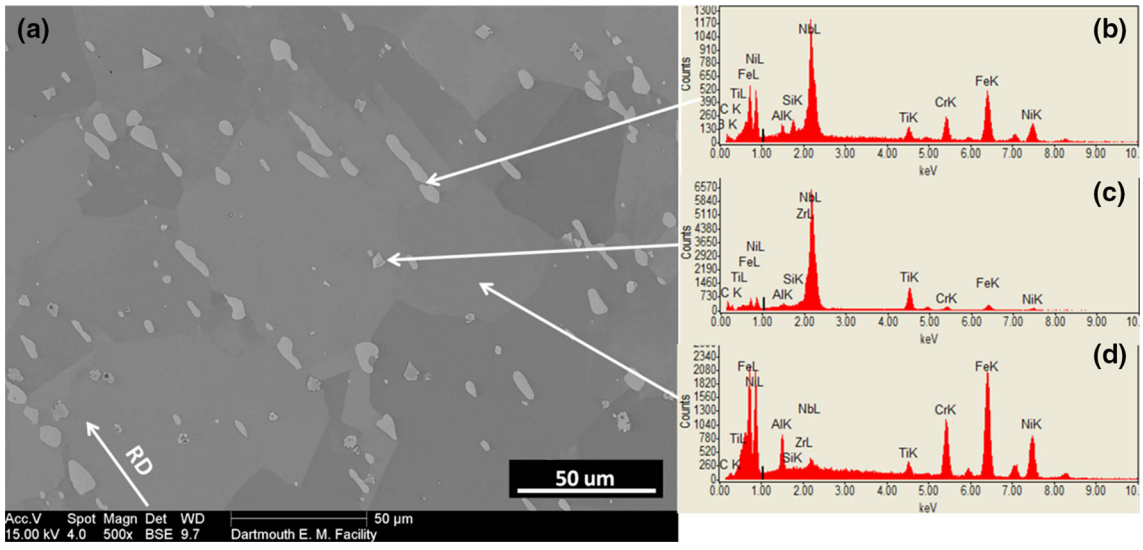

Fig. 2—The BSE image (*a*) of the as-received DAFA29, and EDS from (*b*) and (*c*) niobium-enriched precipitates, and (*d*) the matrix. The rolling direction is indicated.

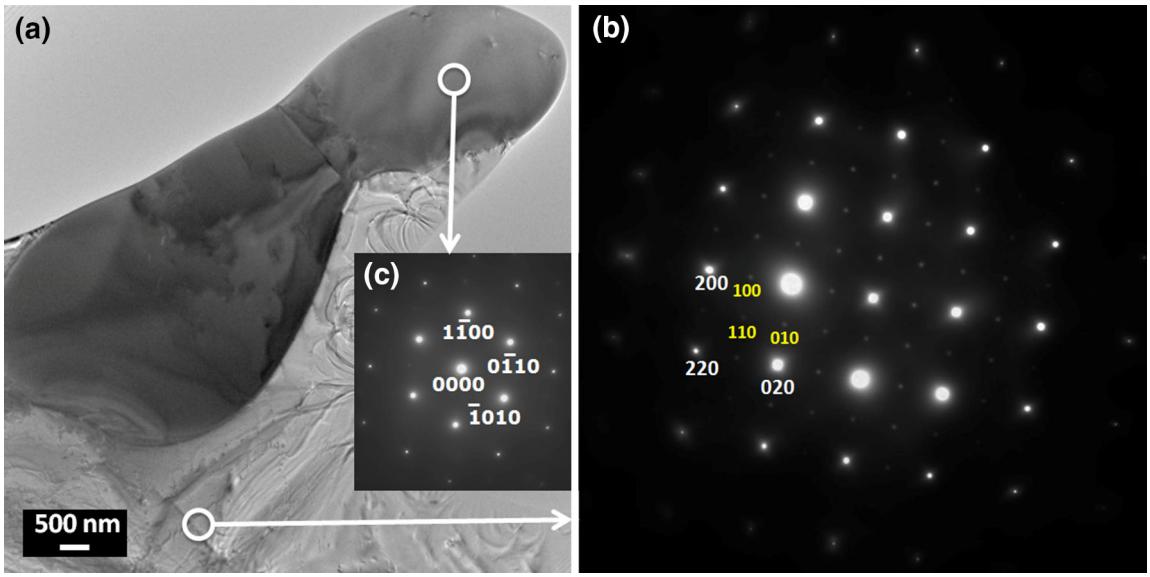

Fig. 3—(*a*) BF TEM image showing a Laves phase precipitate in DAFA29, (*b*) SAD pattern from matrix viewed along [001], and (*c*) CBED pattern of Laves phase precipitate after tilting to [0001].

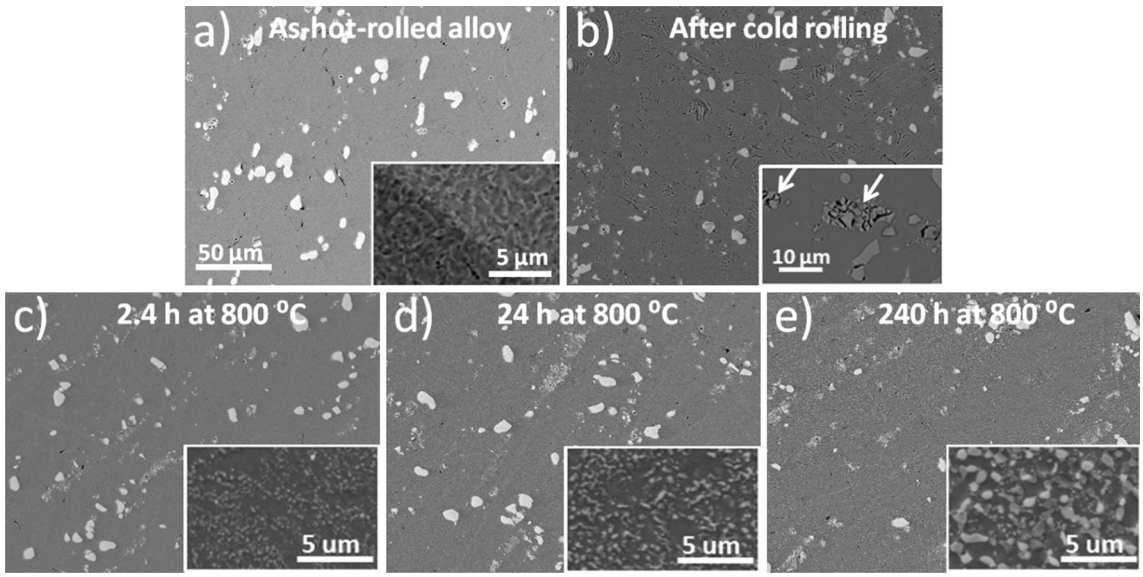

Fig. 4—BSE images of DAFA29 showing fracturing of the Laves phase after cold rolling: (*a*) as received, (*b*) after cold rolling (90 pct thickness reduction), and after annealing at 1073 K (800 °C) for (*c*) 2.4 h, (*d*) 24 h, or (*e*) 240 h.

EDS results (Figure 2(b)), it is confirmed that this precipitate is the Fe_2Nb Laves phase.

B. *Microstructures of Thermo-mechanically Processed DAFA29*

In order to produce fine and uniformly distributed Laves phase precipitates, two thermo-mechanical treatments were used to process DAFA29, as shown in Figure 1. Previous research reported that cold rolling (with 10 pct thickness reduction) of precipitate-strengthened austenitic stainless steels could improve creep properties, because the dislocations introduced by cold rolling acted as nucleation sites for fine MC (NbC) carbide precipitates, resulting in enhanced creep resistance.[12,27,28] It should be noted that the alloys examined here (DAFA29) can be cold rolled to more than 90 pct thickness reduction, indicating that the coarse second-phase precipitates do not degrade room temperature workability of the AFA alloys, similar to the results previously reported in Reference 22.

BSE images of DAFA29 after thermo-mechanical treatment Method #1 are shown in Figure 4. The steel was cold rolled to a 90 pct reduction in thickness, after which it is evident that the large Laves phase precipitates had fractured (Figure 4(b), inset). These samples were then annealed at 1073 K (800 °C) for 2.4 hours (Figure 4(c)), 24 hours (Figure 4(d)), or 240 hours

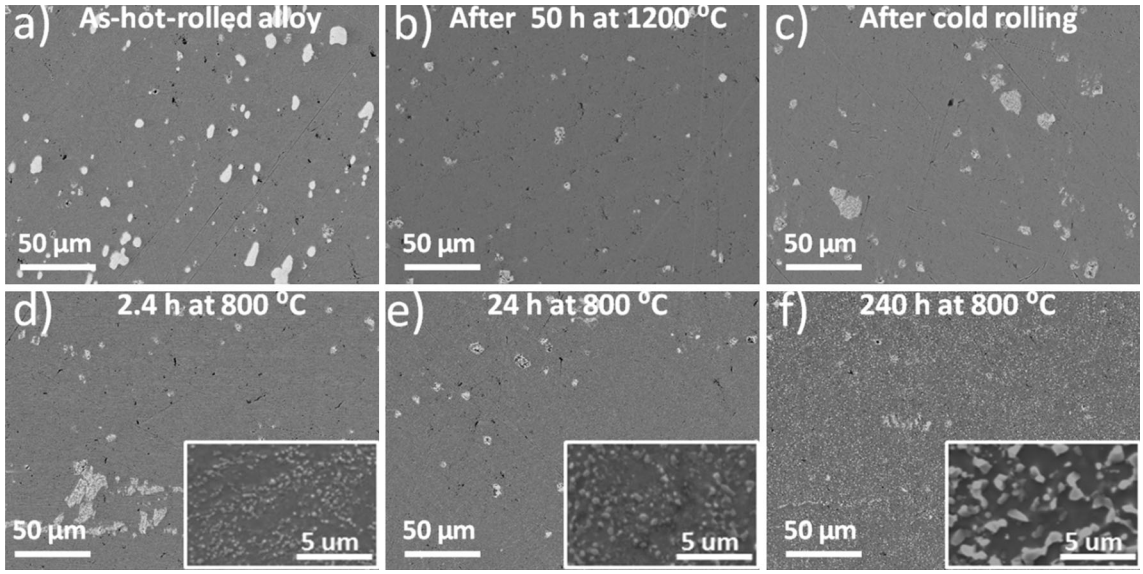

Fig. 5—BSE images of DAFA29: (*a*) as received, (*b*) after a solutionizing anneal of 50 h at 1473 K (1200 °C), (*c*) after a subsequent 90 pct cold rolling reduction, and (c) after solutionizing, cold rolling, and annealing at 1073 K (800 °C) for (*d*) 2.4 h, (*e*) 24 h, or (*f*) 240 h.

(Figure 4(e)). The cold rolling fractured many of the Laves phase precipitates in the matrix resulting in smaller precipitates (Figures 4(c) through (e)).

BSE images of DAFA 29 after thermo-mechanical treatment Method #2 are shown in Figure 5. The aim of using this method is to solutionize the large Laves phase precipitates before cold rolling. Unfortunately, the large Laves phase precipitates could not be completely solutionized at 1473 K (1200 °C), although annealing significantly reduced their volume fraction (compare Figures 5(a) and (b)). The solutionizing anneal also produced a substantial increase in the average grain size from 40 to 250 μm (grain size was measured using the linear line intercept method). As observed for thermo-mechanical treatment Method #1, the residual large Laves phase precipitates also fractured during cold rolling. Upon subsequent annealing, the size of the residual Laves phase precipitates did not change significantly. After the 240 hour anneal, fine-scale particles precipitated out and were evenly distributed in the matrix (Figure 5(f)). These new precipitates presumably nucleated on the dislocations generated during the 90 pct cold rolling. The inset in Figure 5(f) clearly shows precipitates with two different types of brighter contrast, white and light gray, likely due to the presence of two different phase compositions. The light gray phase is likely the Laves phase and the dark gray phase is likely B2 NiAl. These small precipitates were also observed in previous research on AFA alloys.[12,15]

Table II shows the average size of the Laves phase precipitates after both thermo-mechanical treatments using the particle size image analysis technique used by Trotter *et al.*[21] The sizes of the Laves phase precipitates are in the range of 167 to 562 nm, *i.e.*, much smaller than the large Laves phase precipitates in Figures 2 and 3 which are 0.5 to 10 μm. As the annealing time increases from 2.4 to 240 hours, the size of the Laves phase increases from 167 to 417 nm for the samples

Table II. Average Size of Laves Phase Particles Inside of Thermo-mechanical Treated DAFA29

	Average Size (nm)	
Annealing Time (h)	Method #1	Method #2
2.4	166.8 ± 37.1	174.6 ± 44.9
24	237.2 ± 63.6	244.3 ± 64.9
240	417.3 ± 164.9	562.4 ± 172.7

treated by Method #1. The size of the Laves phase in materials treated with Method #2 is slightly larger than those treated by Method #1 for all annealing times. This is due to the extra step of solutionizing in Method #2.

Comparing Figures 4 and 5, the BSE images of the samples after the solutionizing anneal show less Laves phase precipitates. This is especially clear in Figure 5(f), where the large Laves phase precipitates are barely observed. Instead, the small precipitates are uniformly distributed in the matrix. The solutionizing anneal used in Method #2 is an effective way to reduce the size and redistribute the Laves phase precipitates, resulting in a finer and denser distribution. Most of the small Laves phase precipitates appeared to be coupled with B2 NiAl precipitates. Figure 6 shows a BSE image of the precipitates. Based on EDS results, the brighter contrast precipitates are either Laves phase or MC carbides and the darker contrast precipitates are B2 NiAl precipitates. The B2 NiAl normally co-precipitates with the Laves phase during the thermo-mechanical treatment process. Such finer and denser distributed Laves phase and B2 NiAl precipitates (size are less than 1 μm) may be effective in further increasing the creep strength.[22]

BF TEM images and SAD patterns of DAFA 29 after cold rolling and annealing at 1073 K (800 °C) for 2.4, 24, or 240 hour (Method #1) are shown in Figure 7. After the 2.4 hours anneal many small grains with an

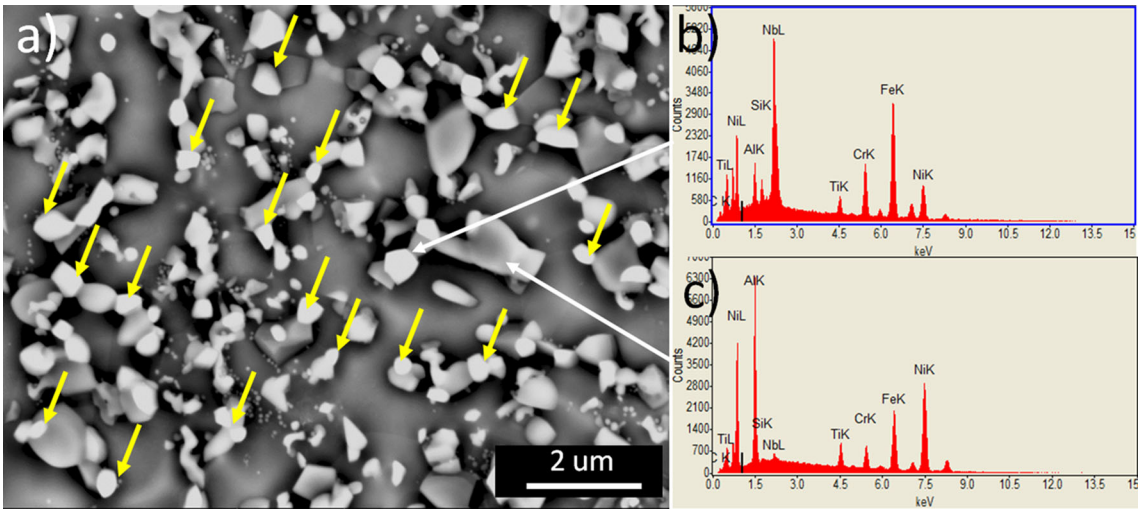

Fig. 6—(*a*) BSE image of DAFA29 after solutionizing annealing 50 h at 1473 K (1200 °C), cold rolling (90 pct) and further annealing at 1073 K (800 °C) for 240 h; (*b*, *c*) are the EDS results from the Laves phase and NiAl precipitates (yellow arrows indicate the Laves phase co-precipitating with the NiAl) (Color figure online).

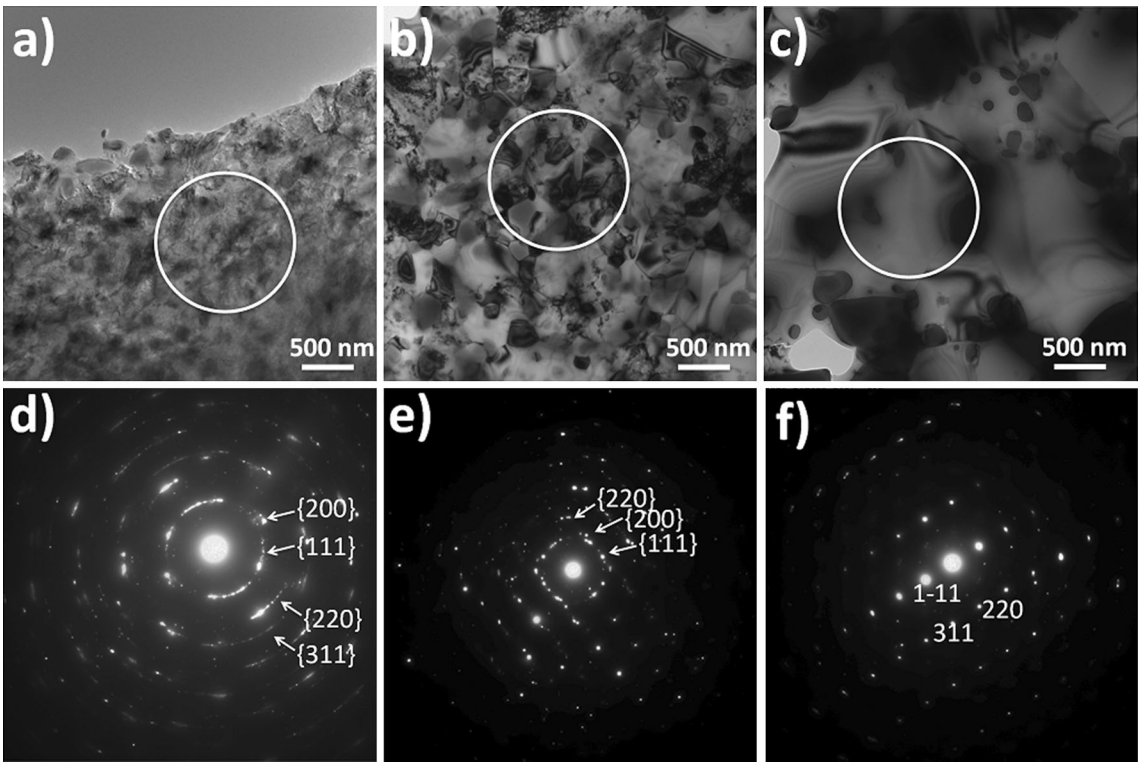

Fig. 7—BF TEM images and SAD patterns of DAFA29 after cold rolling and annealing at 1073 K (800 °C) for (*a*, *d*) 2.4 h, (*b*, *e*) 24 h, or (*c*, *f*) 240 h (Method #1).

average grain size of ~100 nm are present. The SAD pattern shows diffraction rings (Figure 7(d)), a feature characteristic of fine-scale f.c.c. grains having many different orientations. As the annealing time is increased from 2.4 to 240 hours, the grain size increased from ~100 nm to ~1 μm. The diffraction patterns changed accordingly as the number of grains captured within the SAD aperture decreased resulting in a single crystal diffraction pattern from a single grain.

In conventional steels, elongated grains and/or aligned second-phase particles parallel to the rolling direction are developed after large strain cold rolling.[31,32] For the AFA steels, no elongated grains are observed. Instead, a large number of irregular nanoscale grains are observed in TEM images of the 90 pct cold rolled material after 2.4 hours annealing, indicating that all the grains are fully recrystallized after the 2.4 hours annealing process.

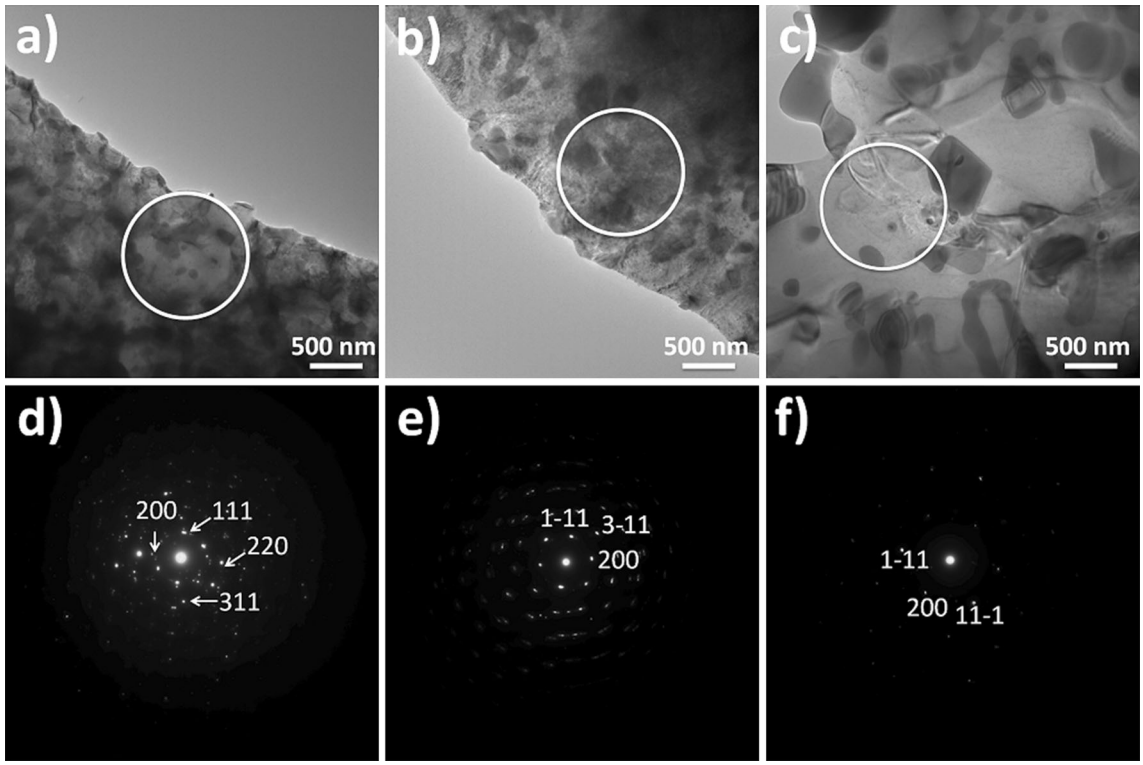

Fig. 8—BF TEM images and SAD patterns of DAFA 29 after solutionizing, cold rolling, and annealing at 1073 K (800 °C) for (*a*, *d*) 2.4 h, (*b*, *e*) 24 h, or (*c*, *f*) 240 h (Method #2).

BF TEM images and SAD patterns of DAFA29 after a solutionizing anneal at 1473 K (1200 °C), cold rolling, and then annealing at 1073 K (800 °C) for 2.4, 24, or 240 hours (Method #2) are shown in Figure 8. For the sample annealed for 2.4 hours, many small grains are observed with an average grain size of ~200 nm with the SAD pattern exhibiting diffraction rings (Figure 8(d)). This is similar to 2.4 hour samples after thermo-mechanical treatment Method #1, where fine grains (~200 nm) are produced by cold rolling and annealing for 2.4 hours. As the annealing time increases from 2.4 to 240 hours, the grain size increases from ~200 nm to ~2 μm.

Comparing Figures 7 and 8, the average grain size produced by Method #2 is ~2 times larger than the grain size produced by Method #1, which is due to grain growth during the solutionizing anneal process. This annealing step increases the average grain size of DAFA29 from 40 to 250 μm.

After thermo-mechanical treatment, the multiple second-phase precipitates in treated DAFA29 were studied by TEM/EDS/CBED.

A BF TEM image and EDS spectrum from a Laves phase precipitate in DAFA29 after thermo-mechanical treatment Method #1 annealed for 240 hours are shown in Figure 9. The Laves phase precipitates appear darker than the matrix in the TEM image due to their greater thickness and/or compositional difference (heavy element Nb), and, hence, greater absorption. The inset in Figure 9(a) shows a CBED pattern from the circled region. The diffraction pattern indicates a hexagonal crystal structure aligned at [0001]. EDS results from the same region of the Laves phase precipitate, Figure 9(b), indicate that it is enriched in Nb and Fe. The EDS data shows an atomic ratio of Fe to Nb of approximately 2:1, consistent with Fe_2Nb precipitates, although the precipitates also contain some other elements.

The creep resistance of the alloys strengthened by Fe_2Nb Laves phase particles alone was previously found to be relatively low at 1023 K (750 °C) and 100 MPa in air, which was attributed to the relatively coarse size of the Fe_2Nb precipitates.[12] Both large size and small size Fe_2Nb precipitates can be observed in DAFA29 after thermo-mechanical treatment Method #1, as shown in Figure 9. These newly formed small Laves phase precipitates (~1 μm) might be helpful to enhance the creep performance.

A BF TEM image and EDS results from a NiAl precipitate in DAFA29 after thermo-mechanical treatment Method #1 and annealed for 240 hours are shown in Figure 10. The CBED pattern in Figure 10(b) inset corresponds to a B2 structure viewed along the [211] zone axis. EDS analysis results from the circled region of the NiAl precipitate are shown in Figure 10(b). Although the precipitates are mostly Ni and Al, they also contain other elements. The NiAl precipitates are observed after both thermo-mechanical treatments. They are not present in the as-received DAFA29. A previous study suggested this B2 phase is likely to increase the creep resistance by affecting dislocation climb in the f.c.c. matrix due to their resistance to dislocation cutting during creep deformation.[15,22]

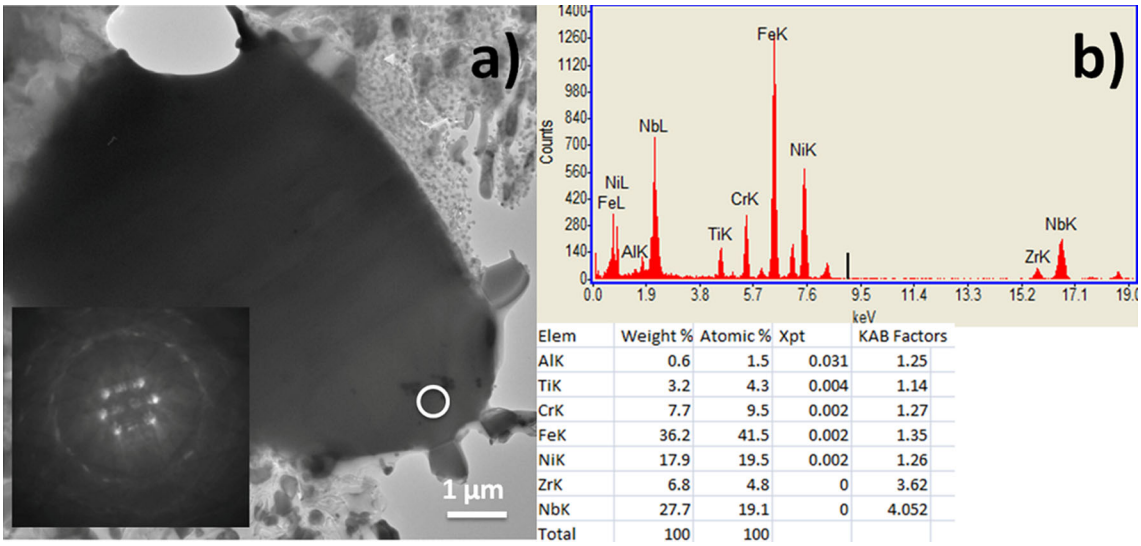

Elem	Weight %	Atomic %	Xpt	KAB Factors
AlK	0.6	1.5	0.031	1.25
TiK	3.2	4.3	0.004	1.14
CrK	7.7	9.5	0.002	1.27
FeK	36.2	41.5	0.002	1.35
NiK	17.9	19.5	0.002	1.26
ZrK	6.8	4.8	0	3.62
NbK	27.7	19.1	0	4.052
Total	100	100		

Fig. 9—BF TEM image (*a*), EDS spectrum (*b*), and CBED pattern from a Fe_2Nb Laves phase precipitate in DAFA29 after thermo-mechanical treatment Method #1, annealed 240 h. The EDS data and CBED pattern are from the region circled in TEM image.

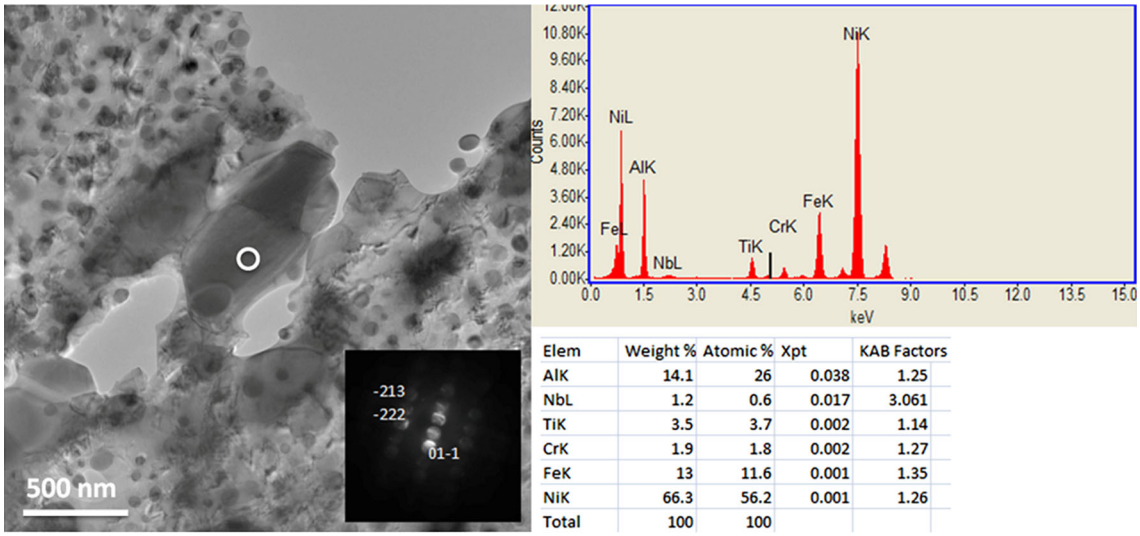

Elem	Weight %	Atomic %	Xpt	KAB Factors
AlK	14.1	26	0.038	1.25
NbL	1.2	0.6	0.017	3.061
TiK	3.5	3.7	0.002	1.14
CrK	1.9	1.8	0.002	1.27
FeK	13	11.6	0.001	1.35
NiK	66.3	56.2	0.001	1.26
Total	100	100		

Fig. 10—BF TEM image (*a*), EDS spectrum (*b*), and CBED pattern for a NiAl precipitate in DAFA29 after thermo-mechanical treatment Method #1, annealed 240 h. The EDS data and CBED pattern are from the region circled in the TEM image.

The B2 phase precipitates also play an important role for the oxidation resistance of the alloy and work as Al reservoirs, which provide Al to maintain the protective alumina scale on the material's surface at high temperature.[22]

A BF TEM image and EDS results from a Ni_3Al precipitate on the edge of a thin foil from DAFA29 after thermo-mechanical treatment Method #1 and annealed 240 hours are shown in Figure 11. The Ni_3Al precipitates are spherical with a diameter less than 100 nm. The inset in Figure 11(a) shows a CBED pattern from the circled region of the Ni_3Al precipitate. This corresponds to a pattern from an $L1_2$ structure viewed along the [212] zone axis. EDS data acquired from the region circled in the TEM image of this precipitate is shown in Figure 11(b). The atomic ratio of Ni to Al(Ti) is approximately 3:1, with small amounts of other elements present.

The average size of the $L1_2$ precipitates in this heat-treated alloy is ~84 nm, which is about eight times larger than in the as-received alloy. These $L1_2$ precipitates have a similar size to the Ni_3Al observed in the AFA alloy after creep tests of 3008 hours at 1023 K (750 °C) and 100 MPa.[20] Besides the spherical $L1_2$ precipitates, no other nanoscale particles, such as carbides or borides, are observed after the thermo-mechanical treatments.

MC carbide (M: Nb, Ti) precipitates are also observed in DAFA29 both before and after thermo-mechanical treatments. Figure 12(a) shows a secondary electron image of MC carbides in one thermo-mechanically

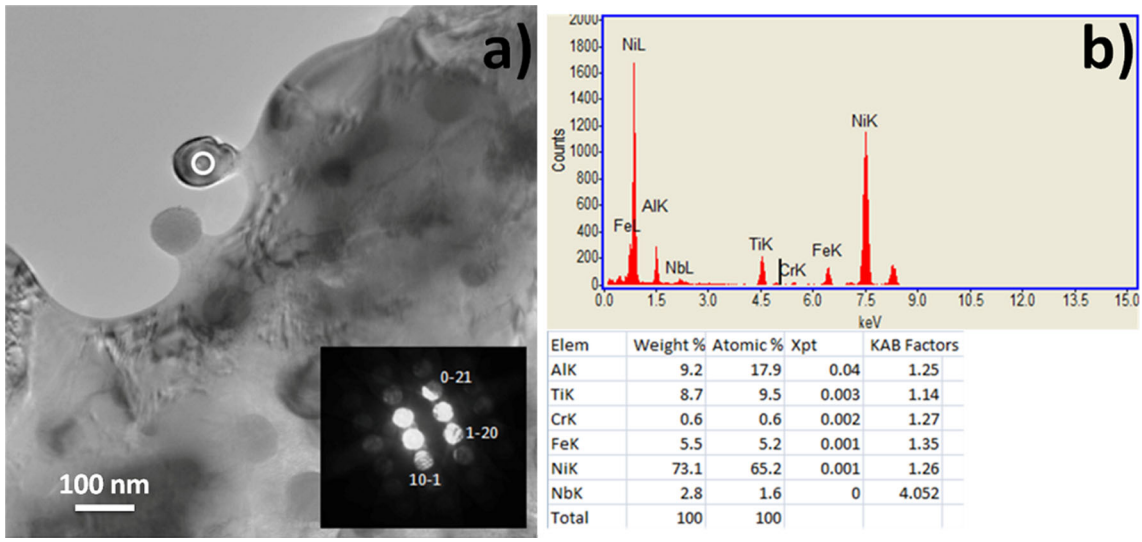

Elem	Weight %	Atomic %	Xpt	KAB Factors
AlK	9.2	17.9	0.04	1.25
TiK	8.7	9.5	0.003	1.14
CrK	0.6	0.6	0.002	1.27
FeK	5.5	5.2	0.001	1.35
NiK	73.1	65.2	0.001	1.26
NbK	2.8	1.6	0	4.052
Total	100	100		

Fig. 11—BF TEM image (*a*), EDS spectrum (*b*), and CBED pattern from a Ni_3Al precipitate in DAFA29 after thermo-mechanical treatment Method #1, annealed 240 h.

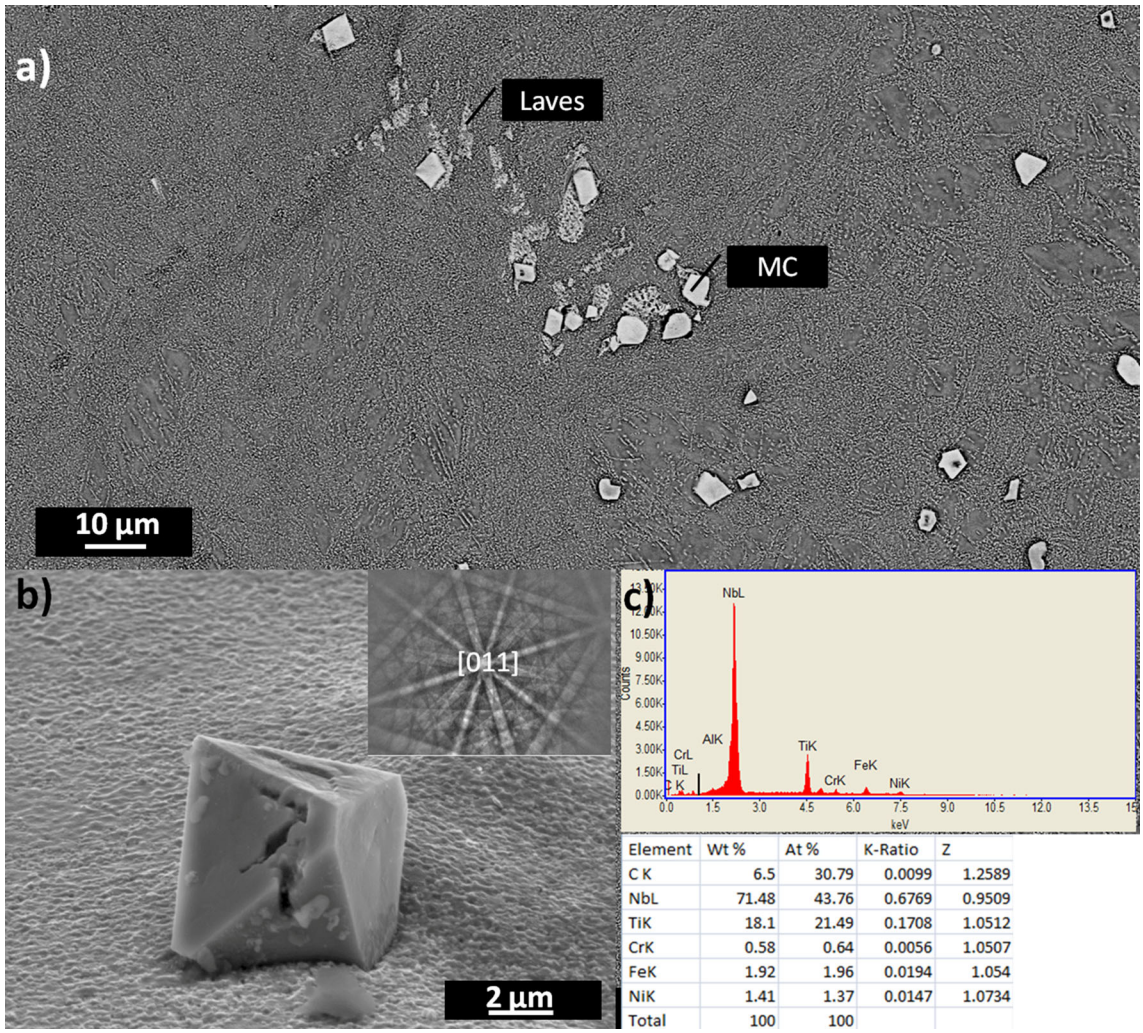

Element	Wt %	At %	K-Ratio	Z
C K	6.5	30.79	0.0099	1.2589
NbL	71.48	43.76	0.6769	0.9509
TiK	18.1	21.49	0.1708	1.0512
CrK	0.58	0.64	0.0056	1.0507
FeK	1.92	1.96	0.0194	1.054
NiK	1.41	1.37	0.0147	1.0734
Total	100	100		

Fig. 12—SEM image (*a*), EDS spectrum (*c*), and EBSD pattern (*b*) from a NbC precipitate in DAFA29 after thermo-mechanical treatment Method #1, annealed 240 h.

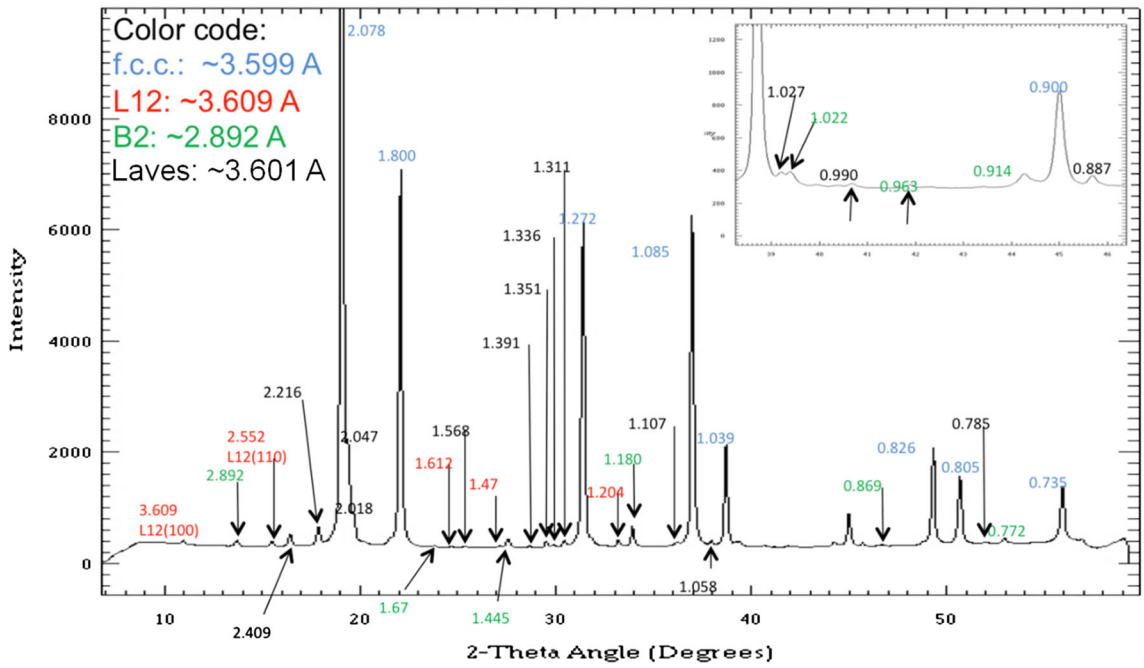

Fig. 13—Synchrotron XRD results for DAFA29 after a 1473 K (1200 °C) solutionizing anneal for 50 h followed by 90 pct cold roll and an 1073 K (800 °C) anneal for 240 h. The inset shows the region from ~38 to ~46 deg expanded.

treated DAFA29 sample. The upper inset in Figure 12(b) is an EBSD pattern, indicating that this is the [011] zone axis of a MC precipitate. Both the pattern and EDS results show this is a MC precipitate.

Since the lattice parameters of the f.c.c. matrix and $L1_2$ precipitates are similar, synchrotron XRD was used to determine their respective lattice parameters in the alloy. Synchrotron XRD results from the DAFA29 samples after a 1473 K (1200 °C) solutionizing anneal for 50 hours, 90 pct cold rolling, and then a 1073 K (800 °C) anneal for 240 hour, are shown in Figure 13. The 240 hour annealed samples were selected for this measurement because the size of precipitates is larger due to particle coarsening, and hence, the XRD signal will be stronger than in the 24 or 2.4 hours annealed samples. In the XRD pattern, the Miller indices of the f.c.c. peaks are labeled in blue, the $L1_2$ superlattice peaks are labeled in red, the Laves phase peaks are labeled in black, and B2 peaks are labeled in green.

The lattice parameters for each phase were calculated based on the highest angle peaks of each phase. The calculated lattice parameters for the phases in the 240 hour annealed sample were 3.609 Å for the L12 phase, 3.599 Å for the f.c.c. matrix, and 2.892 Å for the NiAl phase. The lattice misfit between the $L1_2$ precipitates and the f.c.c. matrix was only 0.28 pct after the 240 hour heat treatment, indicating that very small elastic strain between the precipitates and the f.c.c. matrix is developed.

The room temperature tensile test results for DAFA29 after the two different thermo-mechanical treatments are shown in Figure 14. The samples in Figure 14(a) were cold rolled and then annealed at 1073 K (800 °C) for different time. The yield strength and plastic strain to failure of the as-received DAFA29 are 560 MPa and 22 pct, respectively. The yield strength increased to 1280 MPa and the plastic strain decreased to 5.1 pct after cold rolling and a 2.4 hour anneal. The yield strength decreased with further annealing; the yield strength of the sample after a 24 hour anneal was 1070 MPa, and was reduced to 800 MPa when the sample was annealed for 240 hours. Surprisingly, the strain to failure for all the cold rolled and annealed samples did not change significantly as the annealing time increased and the yield strength decreased.

The samples shown in Figure 14(b) were treated with the additional step of a solutionizing anneal before cold rolling. Again, the yield strength increased to 1150 MPa and the plastic strain decreased to 6.2 pct after this treatment followed by a 2.4 hour anneal. The yield strength decreased to 1020 MPa for an increase in the annealing time to 24 hours, and was further reduced to 750 MPa after an anneal for 240 hours. Again, the strain to failure for the samples treated by this method did not change significantly after cold rolling and different annealing time.

The room temperature yield strengths of these treated DAFA29 specimens are four times higher than previous solution heat-treated AFA alloys and two times higher than the aged AFA alloys studied in Reference 22. This difference is mainly due to the nm-scale or μm-scale grains generated after either thermo-mechanical treatment. Comparison between Figures 14(a) and (b) reveals that the solutionizing anneal is not effective in enhancing the tensile strength of DAFA29, although it is helpful to reduce the size of Laves phase and produce a finer and denser distribution of the Laves phase precipitates.

The tensile test results of the DAFA29 control samples after thermal treatment (Method #1 without

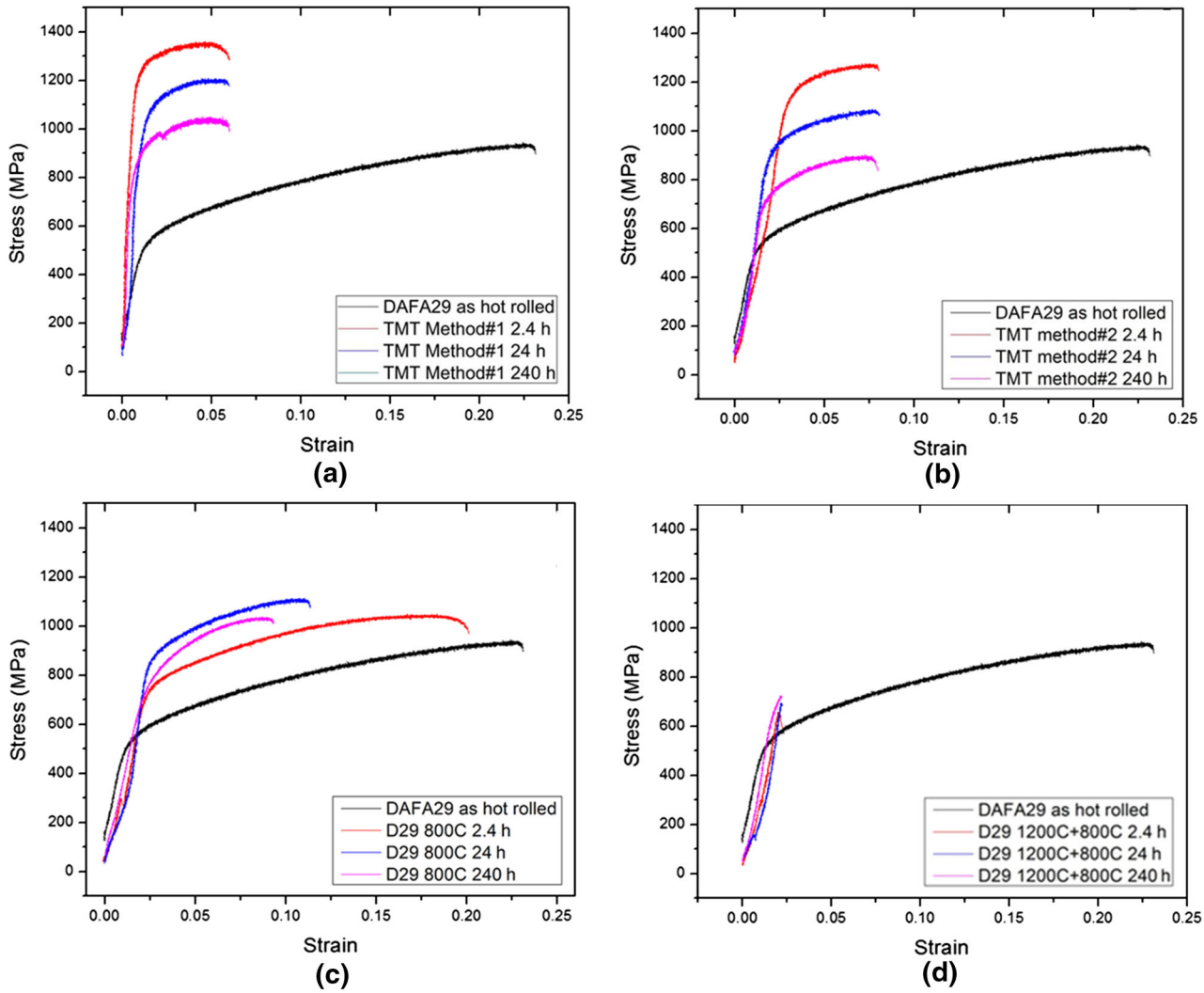

Fig. 14—Tensile test results for DAFA29 after the two different thermo-mechanical treatments. (*a*) Samples are treated under Method #1 compared to the as-hot-rolled DAFA29, (*b*) Samples are treated under Method #2 compared to the as-hot-rolled DAFA29, (*c*) Samples are treated under Method #1 without cold rolling, and (*d*) two-step annealed samples without cold rolling compared to the as-hot-rolled DAFA29.

cold work) are shown in Figure 14(c). Simply, the control samples are annealed at 1073 K (800 °C) for different periods without any cold work. The yield strength increased to 747 MPa from 560 MPa and the plastic strain decreased slightly to 20 pct after a 2.4 hour anneal. The yield strength further increased to 890 MPa and the plastic strain decreased to 10 pct after a 24 hour anneal. For a 240 hour annealing time, the yield strength decreased to 760 MPa, while the plastic strain still continued to decrease to 8 pct.

For comparison, the tensile test results for DAFA29 control samples after using the thermal treatment (Method #2 without cold work) are shown in Figure 14(d). Basically, the control samples are solutionizing anneal at 1473 K (1200 °C) followed by a anneal at 1073 K (800 °C) for different periods without any cold work. The results show that all the samples after this two-step annealing process are brittle and exhibit no plastic strain. The yield strength is slightly higher than that of the as-hot-rolled DAFA29 of 560 MPa.

In order to better understand the correlation between the grain size and the room-temperature mechanical properties obtained, the Hall–Petch relation for the DAFA29 alloys was determined. The yield strength of the thermo-mechanically treated steel obeys a Hall–Petch relationship between the yield strength $\sigma_{0.2}$ and the grain size D, *i.e.*,: $\sigma_y = \sigma_0 + KD^{-0.5}$, where $\sigma_0 = 600$ MPa and $K = 230$ MPa $\mu m^{-0.5}$ according to the linear fit to the yield strength *vs* $D^{-0.5}$. The value of σ_0 differs considerably from that obtained in a 63 pct cold-rolled AISI 301 austenitic stainless steel[33] of 252 MPa (the value of K was 270 MPa $\mu m^{-0.5}$, similar to this work).

The stress σ_0 can be described, in general, as the sum of several strengthening mechanisms: (1) precipitate strengthening (σ_{ppt}), (2) strain hardening (σ_d), and (3)

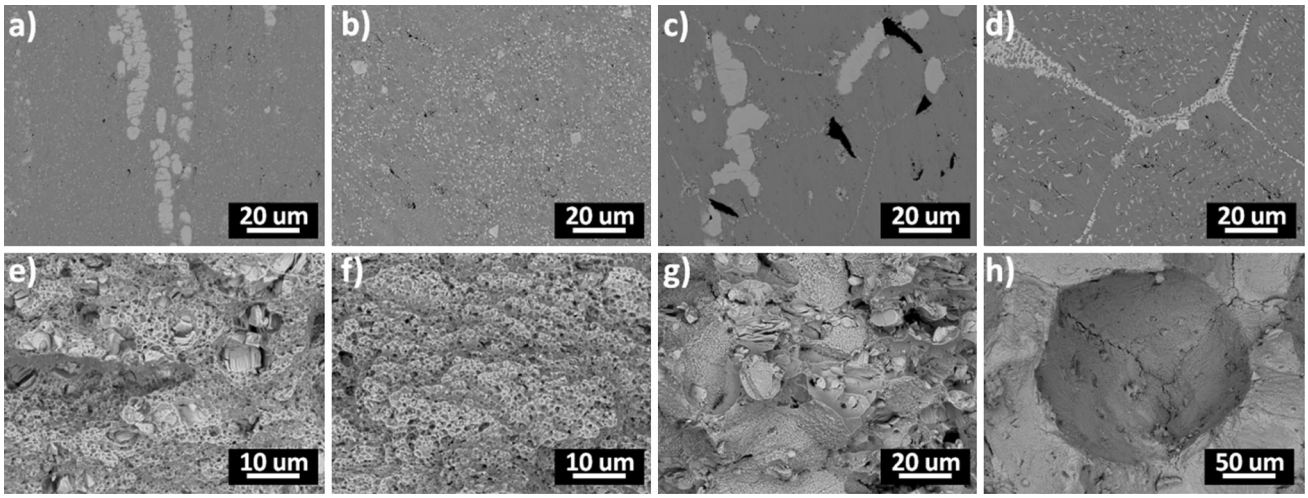

Fig. 15—BSE images of the polished cross section and fracture surfaces of DAFA29 after different thermo-mechanical treatments. (*a*) Method #1 for 240 h, (*b*) Method #2 for 240 h, (*c*) Method #1 without cold rolling, (*d*) Method #2 without cold rolling; (*e*) through (*h*) are the fracture surface for the samples shown in (a) through (d).

solid solution strengthening (σ_{ss}).[33] The off-set stress can be expressed as

$$\sigma_0 = \sigma_{ppt} + \sigma_d + \sigma_{ss}. \quad [1]$$

The large σ_0 observed in the current work likely arises from substantial precipitate strengthening from the finely spaced $L1_2$ Ni_3Al precipitates. The estimated σ_{ppt} is ~289 MPa according to the Eq. [2] and [3] (based on the Orowan looping mechanism) in Reference 34

$$\sigma_{ppt} = 0.84 \cdot \left(\frac{1.2 \cdot G \cdot b}{2 \cdot \pi \cdot L}\right) \cdot \ln\left(\frac{d}{2b}\right), \quad [2]$$

where G is the shear modulus, b is the burgers vector, d is the particle diameter, and L is the particle spacing. For this calculation, a shear modulus of 80,000 MPa and a burgers vector of 2.5×10^{-4} μm were used. The particle diameter used for the calculation is 84 nm.

$$\sigma_{ppt} = \left(\frac{10.8 \cdot f^{1/2}}{d}\right) \cdot \ln\left(\frac{d}{2b}\right), \quad [3]$$

where f is the precipitate volume fraction. The volume fraction of $L1_2$ Ni_3Al precipitates is 21 pct.[20] According to this calculation, the precipitate strengthening σ_{ppt} contributes almost half of the value of the off-set stress σ_0. Note the value of σ_{ppt} is variable and depends on the precipitates size and dislocation-precipitate interaction mechanism.

BSE images of the cross-sections of the strained microstructure for DAFA29 after treatment with Method #1, Method #2, Method #1 without cold rolling, and Method #2 without cold rolling are shown in Figures 15(a) through (d), respectively. Figures 15(e) through (h) are the corresponding BSE images of the fracture surface of those four samples. In the sample treated with Method #1 the large Laves phase fractured perpendicular to the applied stress direction (Figure 15(a)). The fracture surface shows small dimples with Laves and/or B2 phase in the dimple center (Figure 15(e)). Large Laves phase and MC carbide are also observed on fracture surface in this sample. In the sample treated with Method #2 (Figures 15(b) and (f)), the fracture surface shows small dimples similar to Figure 15(e) with size of 1 to 2 μm. In the sample treated with Method #1 without cold rolling (Figures 15(c) and (g)), grain boundary precipitates are generated after annealing for 240 hours. Larger cracks are observed along the grain boundaries. The fracture surface indicates the failures are both on grain boundaries and in the matrix. Both fine grain boundary precipitates and large dimples are observed. For the sample treated with Method #2 without cold rolling (Figures 15(d) and (h)), Laves phase precipitates (exhibiting bright contrast) are present on the grain boundaries and triple junctions (Figure 15(d)). The fracture surface of the materials after the 240 hour anneal, shown in Figure 15(h), show intergranular fracture. This fracture mode of the material is different from the others since the grain boundaries were fully covered by Laves phase and NiAl precipitates. The elongation of this sample is less than 1 pct as shown in Figure 14(d).

IV. CONCLUSIONS

Microstructural analysis and mechanical testing of the recently developed AFA stainless steel alloy DAFA29 have been performed in both the as-received condition and after two series of thermo-mechanical treatments. During these treatments, materials were cold rolled to a 90 pct thickness reduction [both with and without a solutionizing anneal at 1473 K (1200 °C)] and then heat treated at 1073 K (800 °C) for 2.4, 24, or 240 hours.

It was found that

1. A solutionizing anneal at 1473 K (1200 °C) followed by cold rolling and annealing at 1073 K

(800 °C) can be used to generate a finer-scale and more uniform distribution of Laves phase precipitates.
2. The solution anneal produces a large increase in grain size from 40 to 250 μm.
3. The alloy contain Fe_2Nb Laves phase, MC carbide, $Ni_3Al(Ti)$ $L1_2$, and B2 NiAl precipitates after either thermo-mechanical treatment.
4. Cold rolling produces a high density of dislocations, which act as nucleation sites for Fe_2Nb Laves phase, MC carbide, B2 NiAl, and $Ni_3Al(Ti)$ precipitate formation.
5. Nanocrystalline grains are produced after cold rolling and short-time anneals, which grow rapidly to μm-scale size on subsequent annealing at 1073 K (800 °C).
6. Nanocrystalline steels processed through large strain cold rolling exhibit a dramatic increase in yield strength up to 1280 MPa. The yield strength decreases upon further annealing due to grain growth and precipitate coarsening.
7. The yield strength of thermo-mechanically treated AFA steels exhibits a Hall–Petch relationship with a large value for σ_0 that likely arises from precipitate strengthening (σ_{ppt}).

ACKNOWLEDGMENTS

This research was supported by the U.S. Department of Energy under NETL Award DEFG2612FE0 008857. MKM, LY, and atom probe tomography research was conducted through a user project supported by ORNL's Center for Nanophase Materials Sciences (CNMS), which was sponsored by the Scientific User Facilities Division, Office of Basic Energy Sciences, U.S. Department of Energy. Argonne National Laboratory's work was supported under U.S. Department of Energy contract DE-AC02-06CH11357. The authors would like to acknowledge Dr. Yukinori Yamamoto and Dr. Michael P. Brady of ORNL both for providing the AFA stainless steels and for insightful advice. This manuscript has been authored by UT-Battelle, LLC, under Contract No. DE-AC05-00OR22725 with the U.S. Department of Energy. The United States Government retains and the publisher, by accepting the article for publication, acknowledges that the United States Government retains a non-exclusive, paid-up, irrevocable, world-wide license to publish or reproduce the published form of this manuscript, or allow others to do so, for United States Government purposes.

REFERENCES

1. R. Viswanathan and W. Bakker: *J. Mater. Eng. Perform.*, 2001, vol. 10, pp. 81–95.
2. R. Viswanathan and W. Bakker: *J. Mater. Eng. Perform.*, 2001, vol. 10, pp. 96–101.
3. Y. Yamamoto, M.P. Brady, Z.P. Lu, P.J. Maziasz, C.T. Liu, B.A. Pint, K.L. More, H.M. Meyer, and E.A. Payzant: *Science*, 2007, vol. 316, pp. 433–36.
4. V. Ramakrishnan, J. McGurty, and N. Jayaraman: *Oxid. Met.*, 1988, vol. 30, pp. 185–200.
5. D.V.V. Satyanarayana, G. Malakondaiah, and D.S. Sarma: *Mater. Sci. Eng. A*, 2002, vol. 323, pp. 119–28.
6. R. Peraldi, B.A. Pint, and P.J. Maziasz: *Mater. Sci. Forum*, 2004, vol. 461, pp. 815–22.
7. R. Viswanathan, K. Coleman, and U. Rao: *Int. J. Press. Vessels Pip.*, 2006, vol. 83, pp. 778–83.
8. V. Viswanathan, R. Purgert, and P. Rawls: *Adv. Mater. Process.*, 2008, vol. 8, pp. 47–49.
9. R. Viswanathan, R. Purgert, S. Goodstine, J. Tanzosh, G. Stanko, and J. Shingledecker: *Proceedings of the 5th International Conference on Advances in Materials Technology for Fossil Power Plants*, ASM International, Materials Park, 2008.
10. T. Sourmail: *Mater. Sci. Technol.*, 2001, vol. 17, pp. 1–14.
11. M.P. Brady, Y. Yamamoto, M.L. Santella, P.J. Maziasz, B.A. Pint, C.T. Liu, Z.P. Lu, and H. Bei: *JOM*, 2008, vol. 60, pp. 12–18.
12. Y. Yamamoto, M.P. Brady, Z.P. Lu, C.T. Liu, M. Takeyama, P.J. Maziasz, and B.A. Pint: *Metall. Mater. Trans. A*, 2007, vol. 38A, pp. 2737–46.
13. M.P. Brady, Y. Yamamoto, M.L. Santella, and B.A. Pint: *Scripta Mater.*, 2007, vol. 57, pp. 1117–20.
14. Y. Yamamoto, M. Takeyama, Z.P. Lu, C.T. Liu, N.D. Evans, P.J. Maziasz, and M.P. Brady: *Intermetallics*, 2008, vol. 16, pp. 453–62.
15. Y. Yamamoto, M.L. Santella, M.P. Brady, H. Bei, and P.J. Maziasz: *Metall. Mater. Trans. A*, 2009, vol. 40A, pp. 1868–80.
16. M.P. Brady, Y. Yamamoto, M.L. Santella, and L.R. Walker: *Oxid. Met.*, 2009, vol. 72, pp. 311–33.
17. Y. Yamamoto, M.L. Santella, C.T. Liu, N.D. Evans, P.J. Maziasz, and M.P. Brady: *Mater. Sci. Eng. A*, 2009, vol. 524, pp. 176–85.
18. H. Bei, Y. Yamamoto, M.P. Brady, and M.L. Santella: *Mater. Sci. Eng. A*, 2010, vol. 527, pp. 2079–86.
19. M.P. Brady, K.A. Unocic, M.J. Lance, M.L. Santella, Y. Yamamoto, and L.R. Walker: *Oxid. Met.*, 2011, vol. 75, pp. 337–57.
20. Y. Yamamoto, M. Govindarajan, and M.P. Brady: *Scripta Mater.*, 2013, vol. 69, pp. 816–19.
21. G. Trotter, G. Rayner, I. Baker, and P.R. Munroe: *Intermetallics*, 2014, vol. 53, pp. 120–28.
22. Y. Yamamoto, M.P. Brady, M.L. Santella, H. Bei, P.J. Maziasz, and B.A. Pint: *Metall. Mater. Trans. A*, 2011, vol. 42A, pp. 922–31.
23. B.A. Pint, L. Walker, P. Maziasz, M. Brady, Y. Yamamoto, and M. Santella: *Mater. Sci. Forum*, 2008, vol. 595, pp. 725–32.
24. R.C. Reed: *The Superalloys: Fundamentals and Applications*, Cambridge University Press, Cambridge, 2006.
25. H. De Cicco, M.I. Luppo, L.M. Gribaudo, L.M. Gribaudo, and J. Ovejero-García: *Mater. Charact.*, 2004, vol. 52, pp. 85–92.
26. P.J. Maziasz: *JOM*, 1989, vol. 41, pp. 14–20.
27. R.W. Swindeman, P.J. Maziasz, E. Bolling, and J.F. King: *Development and Evaluation of Advanced Austenitic Alloys*, No. CONF-900546-4, Oak Ridge National Laboratory, Oak Ridge, TN, 1990, p. 125.
28. R.W. Swindeman and P.J. Maziasz: *The Effect of MC Forming Additions and 10 Pct Cold Work on the High Temperature Strength of 20Cr-30Ni-Fe Alloys*, Oak Ridge National Laboratory, Oak Ridge, 1991.
29. Y. Yamamoto, G. Muralldharan, and M.P. Brady: US Patent 20,130,266,477, 2013.
30. Z. Cai, B. Lai, W. Yun, P. Ilinski, D. Legnini, J. Maser, and W. Rodrigues: *AIP Conference Proceedings*, 2000, p. 472.
31. T. Sakai, A. Belyakov, R. Kaibyshev, H. Miura, and J.J. Jonas: *Prog. Mater Sci.*, 2014, vol. 60, pp. 130–207.
32. I. Shakhova, V. Dudko, A. Belyakov, K. Tsuzaki, and R. Kaibyshev: *Mater. Sci. Eng. A*, 2012, vol. 545, pp. 176–86.
33. S. Rajasekhara, P. Ferreira, L. Karjalainen, and A. Kyröläinen: *Metall. Mater. Trans. A*, 2007, vol. 38A, pp. 1202–10.
34. J. Moon, M.-H. Jang, J.-Y. Kang, and T.-H. Lee: *Mater. Charact.*, 2014, vol. 87, pp. 12–18.